

Nanospikes on Customized 3D-Printed Titanium Implant Surface Inhibits Bacterial Colonization

Asha Mathew, Jafar Hasan, Sarat Singamneni, and Prasad K.D.V. Yarlagadda*

Additive manufacturing has opened the door to patient-tailored orthopedic implants, which can significantly minimize implant failures associated with prosthesis-to-bone mismatch. Success of an implant also depends on the choice of implant materials, effective osseointegration, implant quality, and the mechanical properties together with its capability to limit infection due to bacterial contamination. Herein, nanospikes are created on 3D-printed titanium-alloyed implant surfaces, which can kill bacteria to minimize any implant-associated infections. For the first time, orthopedic implants with a fracture to the proximal phalanx are fabricated using selective laser melting (SLM) followed by a heat-treatment step and the hydrothermal process. It is showed in the results that by optimizing SLM parameters, dimensionally consistent parts can be produced and tensile properties of the 3D-printed implants can be significantly improved via a simple cyclic heat-treatment process compared to the traditionally manufactured implants. Nanospikes similar to those present on dragonfly wings fabricated on 3D-printed implants surface are able to kill above 90% of adhering bacteria by rupturing the membranes upon contact. These results indicate that fabrication of patient-specific 3D-printed implants with inherent bactericidal properties has the potential to eliminate postsurgical infections and possible implant failures.

1. Introduction


The clinical demand of orthopedic implants has raised tremendously over the past couple of decades with increasing population needing surgeries each year, making it a staple of

medical industry.^[1,2] Orthopedic implants are mostly used for structural reinforcement and are inserted inside body either temporarily or permanently. Temporary implants such as screws and plates are primarily employed for fracture fixation and removed after few months, whereas permanent implants are designed to replace damaged body parts such as hip, knee, ankle, shoulder, or elbow and are expected to stay within the patient throughout the lifespan.^[3,4] Fractures of metacarpals and phalanges are common and in many cases treated nonoperatively if the fracture is stable.^[5] Unstable fractures are operatively treated using internal fixation methods with Kirschner wires (K-wires), pins, screws plates, or a combination.^[6] K-wire fixation creates a biomechanical environment that is stable enough to allow early postoperative mobilization mostly for proximal third and metacarpal neck fractures and is generally associated with better aesthetic outcome than open reduction internal fixation.^[6,7] Plate and screw fixation are considered an ideal option to treat

difficult fractures as it provides absolute construct rigidity compared to other methods of fracture fixation.^[7] The design of medical implants should be very specific to the fractured or damaged bone, especially in plate and screw scenarios, where strategic pores are utilized to promote bone healing in the correct orientation to last for a long time. However, in most cases, standardized implants are bought directly from the manufacturer and modifications are made during surgery by bending, twisting, or trimming the implants to conform to the patient's bone, with verification from the surgeon's judgment.^[4] Manufacturing defect arising from the fabrication process and lack of proper quality control impacts the overall mechanical properties of the implants. Changing critical parameters such as shape, diameter, and length affects the stress distribution in complicated loading scenarios. This highlights the importance of introducing engineered implant to suit specific bone fractures to reduce the likelihood of implant failures.^[8-13] Moreover, traditional methods such as die casting and post-processing computer numerical control milling are expensive processes that require specialized equipment and lead times to manufacture and transport, and hence seldom utilized for patient-specific needs. Unlike traditional manufacturing methods, additive manufacturing (AM) uses a layer-by-layer manufacturing technique allowing fabrication of complex geometries with various materials in a cheaper

A. Mathew, J. Hasan, P. K. D. V. Yarlagadda
School of Mechanical Medical Process Engineering
Queensland University of Technology
2, George Street, Brisbane, QLD 4001, Australia
E-mail: y.prasad@qut.edu.au

S. Singamneni
School of Engineering Computer and Mathematical Sciences
Auckland University of Technology
Auckland 1010, New Zealand

 The ORCID identification number(s) for the author(s) of this article can be found under <https://doi.org/10.1002/adem.202201306>.

© 2022 The Authors. Advanced Engineering Materials published by Wiley-VCH GmbH. This is an open access article under the terms of the Creative Commons Attribution-NonCommercial-NoDerivs License, which permits use and distribution in any medium, provided the original work is properly cited, the use is non-commercial and no modifications or adaptations are made.

DOI: 10.1002/adem.202201306

and faster pace.^[14] The global market of additively manufactured medical devices is rapidly increasing owing to the favorable surgeon–patient outcome along with fabrication ease.^[15,16] Currently, additively manufactured medical implants are applied to various parts of the human body as vascular stents, heart valve prosthesis, artificial joint prosthesis, orthopedic implants such as hips and knees, fracture fixation devices, customized dental crowns, cranial implants, prosthetic limbs, etc.^[15] Choice of implant material is also a key factor to consider while designing an implant. An ideal implant material would be chemically inert, biocompatible, corrosion resistant, and fatigue resistant, and has low elastic modulus. AM allows the fabrication of implants in a range of materials such as polymers, ceramics, composites, and metals. Polymers, ceramics, and composites are mainly used in the fabrication of prosthetic implants, surgical guides, and bone tissue engineering products while metals are primarily used to provide structural reinforcement due to its increased fatigue strength and excellent corrosion properties.^[16–18] Biocompatible titanium alloy (Ti–6Al–4V) exhibiting excellent mechanical properties compared to polymeric materials has recently fallen into this category upon successful fabrication of pentamode meta-materials from Ti–6Al–4V via AM technology.^[19] Currently, titanium alloys are one of the widely used materials for orthopedic implants.^[9]

Implant failures arise due to implant-related infections, peri prosthetic fractures, aseptic loosening, flaws in diagnosis, patient management, poor choice of implants, and inadequate surgical techniques.^[10–13] This creates a significant burden on healthcare in providing the services for surgeries that could have been successful. The surface quality of the additively manufactured implants plays a critical role in determining the success of an implant.^[20] To enhance the biological performance, the surface of additively manufactured implants is either coated with bioactive materials such as hydroxyapatite or chemically roughened using acids or alkalis or mechanically stabilized using shot peening or ultrasonic techniques.^[20] Such surface modifications on AM implants are primarily to promote osseointegration and cell adhesion. A recent retrospective chart review reported major complications for 52.2% of phalanx fractures treated with plate fixation arriving from stiffness, complex regional pain syndrome, infection (8.7%), delayed union, nonunion, malunion, and plate loosening with 30.4% requiring revision surgery.^[21] Therefore, understanding the failure modes is critical in reducing the burden on hospitals and improving patient satisfaction. Fracture-related infections (FRIs) are common complications after fracture fixation and may cause the implant to be rejected by the body and often results in urgent removal.^[22] FRIs are generally caused by Gram-positive bacteria (GPB) such as Staphylococci such as *Staphylococcus aureus* or *Staphylococcus epidermidis* and treated using antibiotics.^[23] Although less common, Gram-negative bacteria (GNB) are responsible for 10–23% of all infections^[24] and is considered to be the most difficult to treat infections, whereas treatment strategies for Staphylococcal implant-associated infections are standardized with high success rate.^[25] GNB infections require long duration of antibiotic treatment (3 months) to combat infection. This process, however, is still causing failures and current research is looking into circumventing bacterial infections via physical measures such as creating “bacteria-killing

nanostructures” on implant surface utilizing techniques such as electron beam lithography, nanoimprint lithography, vacuum casting, reactive ion etching, or hydrothermal synthesis.^[26,27] Such “bacteria-killing nanostructures” are inspired by naturally occurring surfaces, in particular lotus leaves, shark skin, dragonfly wings, and gecko skin.^[26] When bacterial cells come into contact with a nanostructured surface, cell membranes stretch in the regions between the structures, disfiguring the cell wall. If this stretching is sufficient, cell rupture and death occur.^[28] However, in a recent study, Amar et al. indicates that nano-patterned surfaces do not kill bacteria predominantly by rupturing in between protruding pillars but by creating a critical site at the pillar apex leading to significant in-plane strains that may locally rupture and penetrate the cell.^[29]

In our previous work, we have successfully fabricated nanostructures on titanium surfaces to kill bacteria via hydrothermal etching and electron-beam lithography.^[27,30,31] For titanium materials, hydrothermal etching has been identified as the cheapest and most effective method to create nanostructures. This study aims to fabricate nanospikes onto a 3D-printed implant surface and assess its antibacterial efficacy against *Pseudomonas aeruginosa* (*P. aeruginosa*), one of the most difficult to treat GNB. Most 3D-printed implants studied so far are relatively large in size.^[32,33] The 3D printing metallic parts with small, thin curved features with holes is still a challenge. Hence, as a proof of concept, a curved medial/lateral plate was designed for a fracture to the proximal phalanx. We hypothesize that plate loosening can be avoided/minimized by using patient-specific 3D-printed implants and hard to treat GNB infections can be controlled by fabricating nanospikes on implant/plate surface which can kill bacteria upon contact.

2. Results and Discussion

2.1. 3D-Printed Implant Fabrication and Characterization

A curved medial/lateral plate was designed for a fracture to the proximal phalanx using Solidworks and was converted to a patient-specific plate from a computed tomography (CT) scan of a hand using Materialise Mimics and 3-Matic software. The construction steps of the implant design are presented in **Figure 1a–e**. In this study, Ti–6Al–4V powder was chosen as the core material as this is currently the most conventional material for bone medical implants. A total of 60 implants were 3D printed using the Renishaw AM400 SLM system. All implants had a rough finish with high levels of surface granularity (Figure 1f). Out of 60 implants, the surface finish of 59 implants was consistent. Only one implant had a major crack around its edge (Figure S1, Supporting Information).

Such defects may occur with SLM printing technique due to trapped air in the powder causing porosity and pore crystallization of the structure.^[34,35] Thermal stresses can also cause cracking. Figure 1g,h shows front and side profiles of the implant placed onto a representative model of 5th proximal phalanx. The photo illustrates the excellent fit of the implant on the representative model supporting the design and fabrication process. Additive consolidation of metal powders to print parts with complex shapes and thin structural forms to the exact geometrical

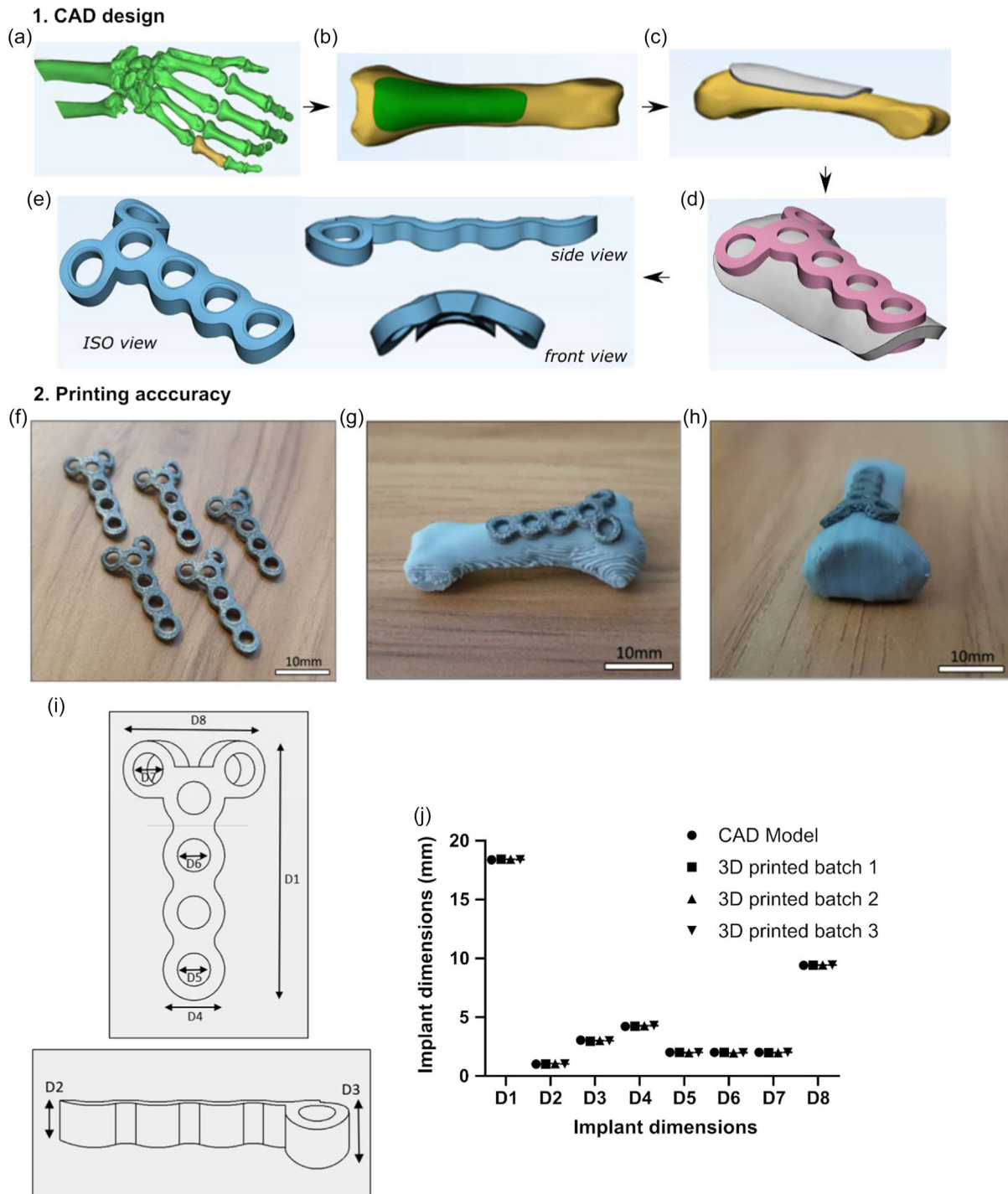


Figure 1. a–e) Steps involved in computer-aided design of 5th proximal phalanx fixation plate. a) Smoothing of computed tomography (CT) scan of a hand was performed using Materialize Mimics software. Then, 6 points of connectivity was applied followed by removal of every other bone except for the 5th proximal phalanx indicated in golden color. b) Highlighted region (green) indicates implant location. c) A thickness of 1 mm given to the highlighted section. d) Traditional implant designed via Solidworks was placed on the surface of 1 mm thick surface on bone, making sure that the implant was protruding from the top and bottom surface. Once in place, a Boolean intersection was performed to create an implant to 5th bone structure of the CT scan. The 0.2 mm fillets were applied to the holes to allow for the bolts to sit within the implant as is industry standard. e) Final design of patient-specific implant. f) Fifth proximal phalanx fixation plate printed via selective laser-melting (SLM) process. g) Front and h) side profiles of the implant placed onto a representative model of 5th proximal phalanx. i) Implant dimension. j) Graph indicates the printing accuracy of SLM process.

topology of the design model remains a challenge, considering the need to use support structures. A reduction in hole size can occur as a result of powder adhesion to the interior walls of the structure, uneven heating, and laser penetration.^[36–38] Under such scenarios, the holes are enlarged, post fabrication, by drilling, so that screws can be inserted accurately. The size of the holes can also be corrected to the required dimensions by calculating the error and enlarging the size of the hole during the design stage.^[36]

As seen in Figure 1i,j, the measurements across 8 different locations of the implant including the regions D5, D6, and D7, which had holes in design, were matching with the initial computer-aided design (CAD) design. Percentage errors for features D5, D6, and D7 with 2 mm diameter in the initial design

were 0.5%, 1.2%, and 0.55%, respectively. Dimensional accuracy of the product was achieved by optimizing the build orientation. A 45° inclined orientation was identified to be the optimum position for this component (Figure S2, Supporting Information). **Figure 2a,b** illustrates the scanning electron microscopy (SEM) images of as-fabricated Ti–6Al–4V implant. Unadhered, adhered and melted microspheres ranging from 20–45 μm were identified on the surface which is typical of SLM process. During SLM process, Ti–6Al–4V powder goes through a repeated melting and solidifying process resulting in the formation of long columnar β grains along the building direction.^[39,40] These β grains are randomly embedded with α' martensite phases due to a faster cooling rate (410 °C s⁻¹) of Ti–6Al–4V.^[41] The presence of martensite phase imparts poor mechanical properties

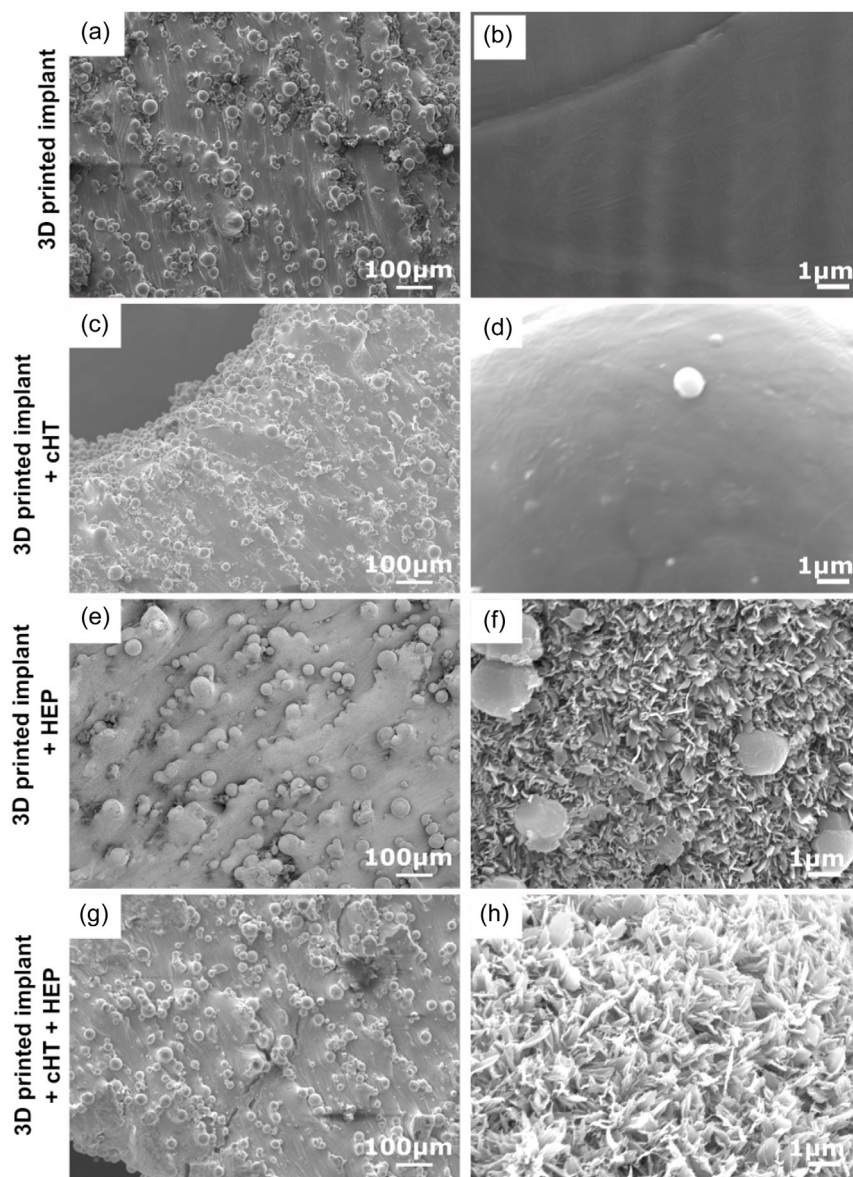


Figure 2. Scanning electron microscopy (SEM) images showing the surface of a,b) SLM-printed implant, c,d) SLM-printed implant post cyclic heat treatment (cHT), e,f) nanospike formation on the surface of SLM-printed implant without cHT and post hydrothermal etching process (HEP), and g,h) nanospike formation on the surface of SLM-printed implant post cHT and HEP treatment.

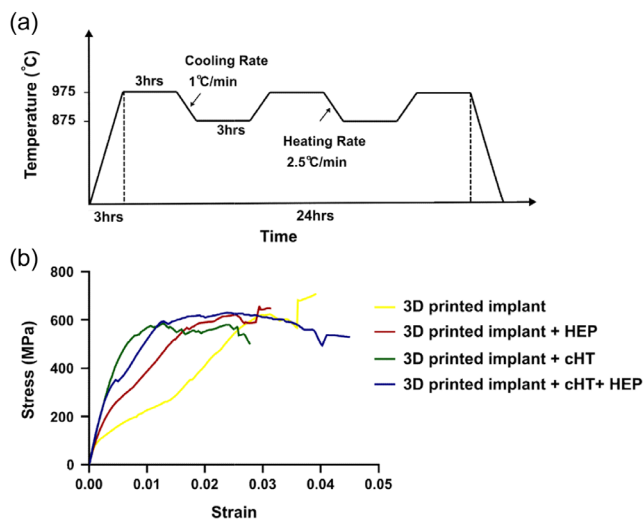


Figure 3. a) Schematic of cHT-involving thermal cycling between 975 and 875 °C with heating rate of 2.5 °C min⁻¹ and cooling rate of 1 °C min⁻¹ for 24 h. b) Stress–strain curves for as printed 3D-printed implants, 3D-printed implants post HEP, 3D-printed implants post cHT and 3D-printed implants post cHT and HEP derived from tensile mechanical testing.

such as reduced strength and toughness.^[42] Hence, a cyclic heat treatment (cHT) was performed on the implants (Figure 3a).

The SEM images of the implant surface post cHT are represented in Figure 2c,d. Nanospikes were formed on the surface 3D-printed samples following hydrothermal etching process (HEP). The surface topography of the nanospikes generated via HEP with or without cHT is represented in Figure 2e–h. Nanospikes formed on 3D-printed surface with or without cHT were similar in morphology. During hydrothermal process, the surface of 3D-printed titanium was first converted into oxide and then etched by the dissolution of titanium and growth of titanium oxides to form nanospikes.^[43] These nanospikes were randomly spaced and were distinct from one another in length and orientation. The average length of the nanospike was around 403 ± 117 nm, base diameter 40 ± 4 nm, and tip diameter 8 ± 5 nm. The irregular shape of the nanospikes formed from the HEP resembled the surface topography of dragonfly wing surface.^[26] The length and shape of the TiO₂ nanospikes was attributed by the sodium hydroxide (NaOH) concentration (1 M), reaction time (2 h), and reaction temperature (180 °C) employed in this study. Our previous studies have shown that the size and shape of the nanostructures can be varied changing the concentration of NaOH, reaction time, and temperature.^[44] X-ray diffraction spectroscopy indicates the presence of anatase TiO₂ nano-crystallites upon HEP (Figure S3, Supporting Information).

Figure 3b shows the stress–strain curves of 3D-printed implants with or without cHT and HEP. It can be seen from the figure that all test samples exhibit i) an initial elastic region, ii) a plateau to a plastic region, and then iii) a steep decline to a fracture point. The Young's modulus of Ti–6Al–4V produced by a traditional manufacturing process (excluding AM process) is around 110 GPa.^[45,46] This was used to compare the Young's modulus that is developed in the elastic regions of the stress–

Table 1. Tensile test results showing young's modulus, yield strength (YS), and ultimate tensile strength (UTS).

Samples	Young's modulus [GPa]	YS [MPa]	UTS [MPa]
3D-printed implant	88.6 ± 0.014	686.96 ± 65.1	724.9 ± 110.7
3D-printed implant + HEP	87.5 ± 0.320	632.6 ± 149.1	640.528 ± 163.9
3D-printed implant + cHT	109 ± 0.499	654.9 ± 106.6	655.5 ± 30.64
3D-printed implant + cHT + HEP	105 ± 0.282	742.6 ± 109.9	797.9 ± 92.28

strain graphs for each of the test sample. The elastic region of the graphs is identifiable by the linear relationship between the strain and stress before any significant plateauing effect happens. Young's modulus is the gradient of this linear relationship and will identify if the implants are comparable to each other. Table 1 shows the average Young's modulus (gradient) of the linear section of each of the test set. The 3D-printed samples before cHT displayed reduced modulus values (88.5 ± 0.014 GPa), compared to the conventional manufacturing process. Porosity, residual stress and cracks within the prints are attributing to the weaker mechanical properties of titanium compared to traditional process. It was observed that upon cHT, the Young's modulus of 3D-printed samples were around 109 ± 0.499 GPa significantly higher than as printed parts ($p \leq 0.0001$) (Table 1). The heat-treatment cycle reduces the residual stress from printing and creates a globularized microstructure improving the strength of the materials.^[47] Interestingly, it was also noted that HEP was slightly reducing the modulus values, with 3D-printed implants with HEP treatment and 3D-printed implants with cHT and HEP displaying Young's modulus around 87.5 ± 0.32 and 104 ± 0.28 GPa, respectively. cHT and HEP did not significantly affect the yield strength (YS) and ultimate tensile strength (UTS) of the 3D-printed implants. However, UTS values under tensile loading of all samples were in the range of 640–790 MPa, which were lower compared to previous reports (1017–1274 MPa).^[47] This might be due to the thin intrinsic porous structure of the implants compared to conventionally used dog bone specimen. Although traditionally manufactured titanium parts impart superior mechanical properties compared to 3D-printed parts, it should be noted that all 3D-printed implants with or without heat treatment were able to withstand load around 800 N, which is reasonably high for finger implants for its intended purpose.

2.2. Antibacterial Performance of Surface Modified 3D-Printed Implants

The bactericidal efficacy of the 3D-printed implants upon surface modification with nanospikes was evaluated against *P. aeruginosa*, hard to treat GNB. Results indicate that 94.2% ± 5.3% of bacterial cells were killed upon its interaction with the sharp nanospikes within 2 h of incubation while both 3D-printed implant surface and flat Ti6Al4V surface did not exhibit any significant (1.5% ± 2.5% and 2.8% ± 1.01% killing) bactericidal properties (Figure 4a–c,e). Bacterial attachment on flat,

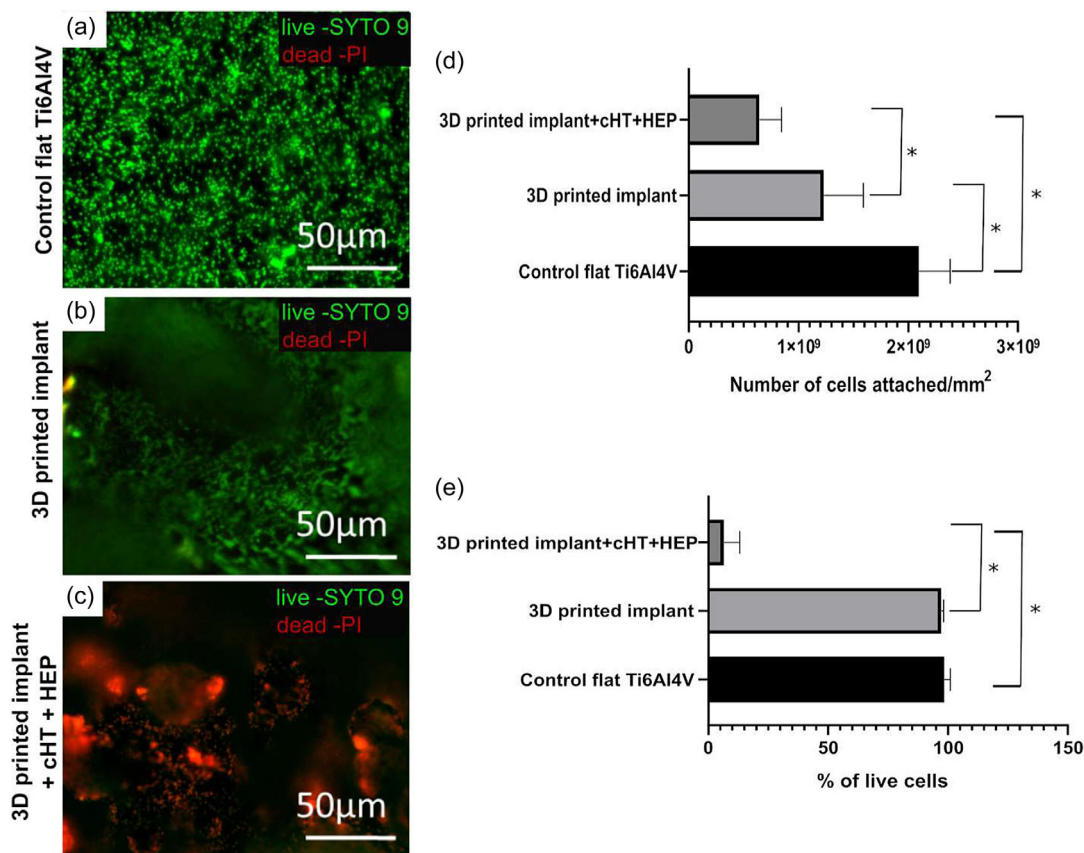


Figure 4. Fluorescent microscopy images revealing the viability of the attached *Pseudomonas aeruginosa* on flat Ti6Al4V surface. a) The 3D-printed surface b) and nanospike-modified 3D-printed surface. c) The live cells are stained green, whereas dead cells are stained red. d) Significant reduction in attachment of *P. aeruginosa* on nanospike-modified surface and as such 3D-printed surface compared to flat surface. e) Viability analysis showing percent of viable bacterial cells on flat, 3D-printed and nanospike-modified surface calculated using fluorescent signals from the LIVE/DEAD stains. Results indicate significant bactericidal efficiency of nanospike-modified surface compared to nonmodified surfaces.

3D-printed, and nanospike-modified 3D-printed surfaces were $20.9 \times 108 \pm 2.8 \times 108$, $12.3 \times 108 \pm 3.6 \times 108$ and $6.4 \times 108 \pm 2.0 \times 108$ cells mm^{-2} , respectively (Figure 4d). Interestingly, bacterial attachment on 3D-printed surface was significantly lower than flat Ti6Al4V. Results also indicate that the attachment of bacteria on to nanospiked surfaces was also significantly reduced ($p \leq 0.0001$) compared to flat Ti6Al4V and 3D-printed surface. Figure 5 represents the SEM images of *P. aeruginosa* attachment onto flat Ti6Al4V, 3D-printed implant surface, and 3D-printed implant surface post HEP within 2 h of contact. The sharp apex of nanospikes formed via HEP appeared to penetrate the cell wall and rupture the cell membrane, eventually killing the bacterial cells. Figure 5f clearly demonstrates the penetration of nanospikes through several locations on the single bacterial cell membrane within 2 h of contact which is attributed to turgor loss.^[48] It is worth to note that the bactericidal efficiency of nanospiked surface on 3D-printed parts is higher than the previously reported flat surfaces with thinner and sharper nanostructures.^[30,31,49]

When cells were left for 18 h on the nanospiked implant surface, almost all cell which came into contact with the implant surface got lysed (Figure 6). Lysed cell get sunk into the

nanospikes as shown in Figure 6a, allowing more room for further cell death. Certain areas of the implant displayed multiple layers of cell death as shown in Figure 6b indicating the efficacy of nanospikes against GNB. Even after multiple layer of cell death, nanospikes were still visible on the implant surface. In addition to thinner, sharper, and randomly spaced nanospikes, the presence of microspheres on 3D-printed surface can generate randomly orientated nanospikes. Having nanospikes in all directions will increase the chance of bacterial contact with the nanospikes. Such tip-localized mechanism rules the major proportion of the cell–nanospike interaction especially for multidrug-resistant Gram-negative strains like *P. aeruginosa*.^[49] The rod-shape structure of *P. aeruginosa* enables multiple nanospike contact points within a single cell. Hence, upon contact with the sharp apex of the nanospike, the thin peptidoglycan layer (≈ 2.5 nm) of *P. aeruginosa* is easily deformed and penetrated into the nanospike. This mechanism triggers the production of reactive oxygen species (ROS) resulting in increased levels of oxidative stress proteins within cells leading to cell death. Cell–nanospike interaction mechanism can also inhibit bacterial cell division eliminating the chances of biofilm formation.^[50,51]

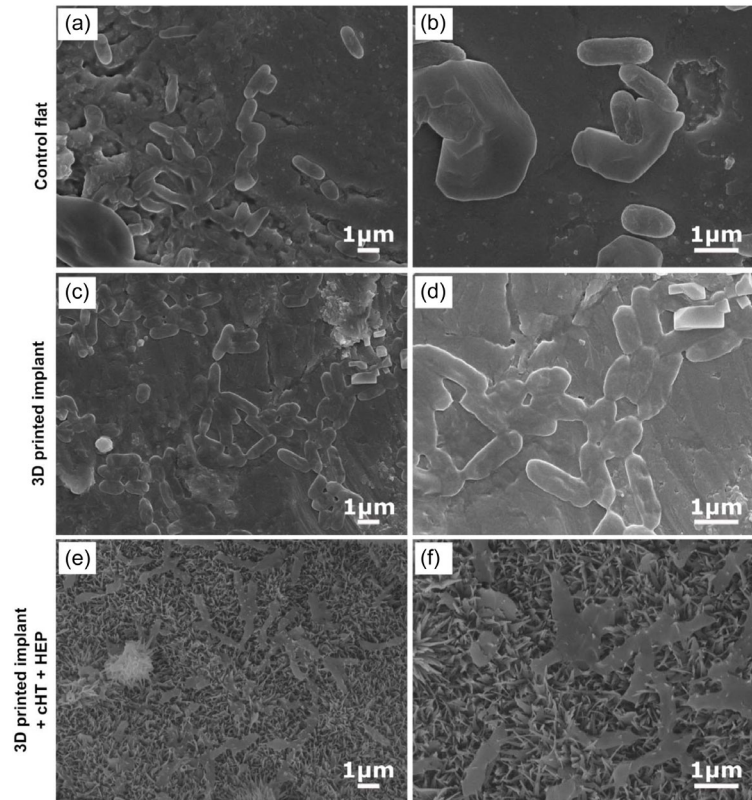


Figure 5. SEM images of *P. aeruginosa* adhesion on to various Ti6Al4V plates after 2 h incubation. a,b) Bacterial cell adheres significantly higher on flat Ti6Al4V plates, showing viable cells with no indication of distress or change in morphology. c,d) Bacterial cells also adhere onto 3D-printed surface with less cell density compared to flat surface also displaying no change in morphology indicating healthy viable cell. e,f) Bacteria-killing efficiency of nanospike surface is demonstrated. Bacterial cell membrane is punctured at various location within the single cell demonstrating total loss of turgor.

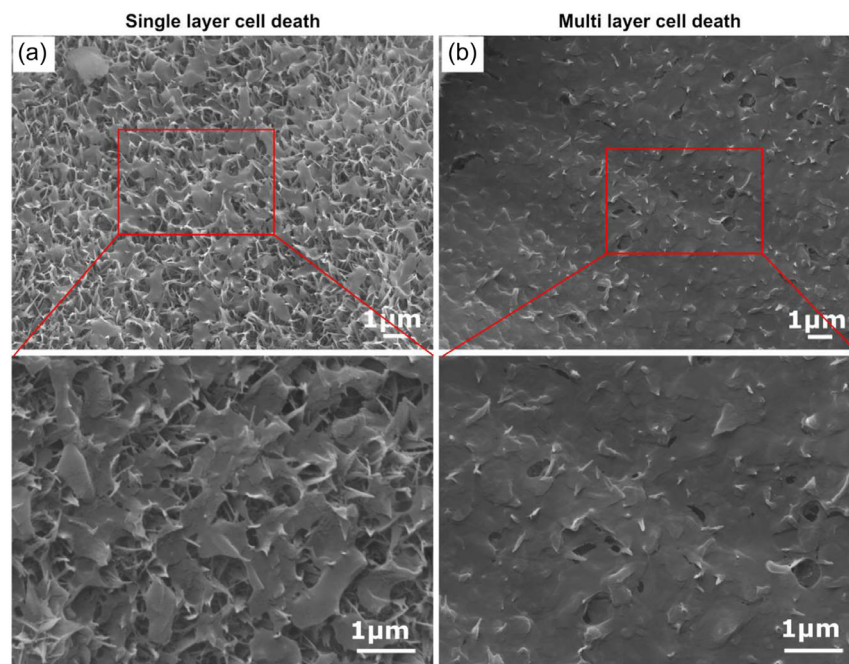


Figure 6. Bactericidal efficacy of nanospiked 3D-printed implant surface. SEM images showing *P. aeruginosa* cell death after 18 h incubation. a) Single-layer cell death and b) multilayer cell death.

3. Conclusion

In summary, patient-specific curved medial/lateral plate was fabricated via SLM technology for a fracture to the proximal phalanx. Using the advanced additive metal-processing method SLM and by optimizing the build orientation, we were able to produce personalized implants with the high-dimensional accuracies. Young's moduli values similar to conventional fabrication method were achieved on 3D-printed parts through a cHT process, overcoming one of the major drawbacks of the AM process. Nanospikes similar to those found on dragon fly wings were successfully fabricated on 3D-printed patient-specific lateral plates via hydrothermal etching process. These bio-inspired nanospikes were able to kill more than 90% of bacteria efficiently within 2 h of contact and were able to kill multiple layers of bacteria within 18 h. Such antibacterial personalized implants can significantly reduce prosthetic joint infections caused by multidrug-resistant Gram-negative strain and side effects caused by long-term antibiotic use. Healthcare industry burden can thereby be minimized by saving millions of dollars spent on the cost of treatment and complex revision surgery and will also aid patients seeking implant surgery, by improving their quality of life.

4. Experimental Section

Implant Design and Fabrication: Computed tomography (CT) scans of model hand were provided by Metro North Hospital. Using Solidworks, a 3D model of the traditional implant was first designed. Utilizing Materialise Mimics, 3-Matic software, and the threshold tool, bone was identified, and a mesh was created from the imported CT scans. The 5th Proximal Phalanx was identified and recalculated as an object. This object was then used in the personalization of the implant design. Using the final CAD files, Ti6Al4V implants were printed based on the Renishaw AM400 SLM system at the AM research Centre, Auckland University of Technology, Auckland. The Ti6Al4V alloy powders with an average particle size of 30 μm were sourced from Renishaw. SLM chamber was maintained at room temperature and filled with Argon, maintaining the O_2 level at 0%. The critical process parameters used are as listed in Table S1, Supporting Information. Considering the thin structural form of the implant, it was a challenge to find the optimal orientation for the build direction, where the need for the support structures is minimized. After a few trials, a 45° inclined orientation with the build plate was identified to be the optimum orientation for the part over the build platform with which, the support structures were minimized and confined only to the bottom most strand of the structure, attaching it to the build plate. These minimal support structures were easily removed once the printing and post-process handling were completed.

Heat Treatment of Implants: Following the 3D-printing process, a cHT was undergone to generate a microstructure (Figure 2b). Briefly, the sample was heated in a furnace to 975 °C at a heating rate of 5 °C min^{-1} after which thermal cycling was employed for 24 h between 975 and 875 °C at a cooling rate of 1 °C min^{-1} and heating rate of 2.5 °C min^{-1} .

Fabrication of Nanospikes on 3D-Printed Implant Surface: Following heat treatment, implants were undergone HEP to generate nanospikes on implant surface as we previously described with slight modifications.^[23] Briefly, 3D-printed titanium implants were first rinsed three times in ethanol and dried with N_2 gas. Implants were placed in a custom-made polytetrafluoroethylene holder (with implants leaning on an angle) in a 125 mL Parr acid digestion vessel, with 50–60 mL 1 M NaOH. The sealed vessel was placed in the oven (Thermoline Scientific) and temperature increased to the specified reaction temperature. Start time was recorded as the time when the oven had reached temperature and was stable without fluctuation. After the given reaction time (2 h at 180 °C), implants were removed

from the oven and cooled inside a fume hood. When completely cooled, implants were removed from the vessel, rinsed three times in 18.2 M Ω H_2O and dried with N_2 gas. Implants were then placed in a furnace and annealed for 1 h at 300 °C (10 °C min^{-1} heating rate), and removed when furnace temperature had cooled below 80 °C. Once at room temperature, implants were submerged in 20 mL of 0.6 M hydrochloric acid solution for 30 min, to exchange ions. After this step, implants were once again rinsed three times in 18.2 M Ω H_2O and dried with N_2 gas. The final step of fabrication was to calcine the implants in the furnace for 2 h at 600 °C (10 °C min^{-1} heating rate). Implants were left to cool in the furnace and were removed when the temperature reached below 80 °C and stored in an airtight container until further use.

Physical Inspection: The physical inspection of the implants followed 2 main processes. First, the implants where visually inspected to identify any defects such as cracks or anomalies on the surface finish to ensure consistency of implant quality. Second, photos were taken of the implant and the 3D-printed replica of proximal phalanx surface highlighting the patient-specific design.

Dimensional Accuracy: Dimensional accuracy of implants was analyzed over 30 implants printed in 3 different batches. The 30 implants were individually measured in x, y, and z direction using a digital Vernier Caliper with an accuracy of 0.01 mm to ensure consistency of SLM printing technology. Eight different dimensions ranging from the length of the implant to the holes were considered critical for the implant to function in the plate and screw configuration (Figure 1h). This will allow for critical analysis between different batches, with the same manufacturing conditions and the 3D CAD model.

Microstructure Analysis: Microstructure of the 3D-printed implants was analyzed using SEM. Samples were gold coated and images were taken using the Jeol JSM-7001F SEM at an accelerated voltage of 15 kV.

Mechanical Testing: The tensile properties of the 3D-printed implants with or without cHT and HEP were tested using Instron 5567. Four implants from each group were taken to 2% elongation of the original length, which is equivalent to a 0.4 mm of extension when placed in the Instron5567 at a displacement rate of 1 mm min^{-1} .

Antibacterial Testing: The 3D-printed implants with or without surface modification with HEP was tested against *P. aeruginosa* (obtained from the American Type Culture Collection [ATCC], ATCC 27 853). Flat Ti-6Al-4V plates were used as the control. Antibacterial testing was performed as per previously described protocol.^[46] Briefly, all test samples were soaked in ethanol for 20 min, dried under fume hood and ultraviolet sterilized prior to testing. Refreshed *P. aeruginosa* cultures were grown in 5 mL of sterile nutrient broth (Oxoid) at 37 °C with overnight shaking at 180 rpm in an orbital shaker. At the logarithmic growth phase, bacterial suspension was adjusted OD600 to 0.1 and further diluted (1:100) in sterile phosphate-buffered saline (PBS). The 500 μL of bacteria suspension in PBS was added onto each sample and incubated for 2 or 18 h at 37 °C in an orbital shaker at 80 rpm. Bactericidal properties of the implant surface were characterized using LIVE/DEAD assay and SEM imaging.

The viability analysis of the adherent *P. aeruginosa* on 3D-printed implants and control surface was determined by staining the cells with LIVE/DEAD BacLight Bacterial Viability kit (Molecular Probes, Invitrogen). Staining solution was prepared as per manufacturer's instructions. Briefly, 5 μL of propidium iodide (PI, 30 mM or 20 mg mL^{-1} in dimethyl sulfoxide [DMSO]) and 5 μL of SYTO 9 dye (5 mM in DMSO) were added to 1 mL 0.8% sodium chloride (NaCl) buffer. After 2 h of incubation with bacterial cell, 3D-printed implant with or without surface modification and the control flat Ti-6Al-4V plate were gently washed with 0.8% NaCl buffer and incubated with staining solution for 15 min and imaged using fluorescent microscopy (inverted Nikon Eclipse TI-S microscope) for live (green—SYTO 9) and dead (red—PI) cells. Quantification of LIVE/DEAD assay was performed using Image J software. Fraction of viable and nonviable cells was determined by counting the cells stained as both green and red in color from 5 images of at least four independent replicates.

For SEM imaging, the bacterial suspension was removed after 2 or 18 h of incubation, rinsed gently with PBS and fixed using 3% glutaraldehyde

over 2 h. Samples were then washed in 0.1 M cacodylate buffer, 1% osmium tetroxide, ethanol series (from 50% to 100%), and lastly with hexamethyldisiloxane. Samples were gold coated and images were taken using the Jeol JSM-7001F SEM at an accelerated voltage of 15 kV. Antibacterial tests were performed twice with at least four samples per group for each test. Statistical analysis was performed by using a one-way ANOVA Tukey's multiple comparison test. Significant results are indicated in the figures, where $*p < 0.0001$.

Supporting Information

Supporting Information is available from the Wiley Online Library or from the author.

Acknowledgements

The authors gratefully acknowledge Bradley Nicholls for his aidance with the CAD design and mechanical testing. The authors would like to thank Nick Green for providing CT scans of hand and initial guidance on using Materialise Mimics and 3-Matic software. Authors would like to acknowledge the facilities at the Central Analytical Research Facility (CARF), especially Tony Wang for performing XRD (CARF), Centre of Biomedical Technologies (CBT) at Queensland University of Technology, Australia, and Additive Manufacturing Research Centre, Auckland University of Technology, Auckland for the use of their equipment.

Open access publishing facilitated by Queensland University of Technology, as part of the Wiley - Queensland University of Technology agreement via the Council of Australian University Librarians.

Conflict of Interest

The authors declare no conflict of interest.

Data Availability Statement

The data that support the findings of this study are available from the corresponding author upon reasonable request.

Keywords

additive manufacturing, antibacterial surface, nanofabrication, proximal phalanx implants

Received: September 8, 2022

Revised: December 3, 2022

Published online: January 18, 2023

- [1] R. Bahr, B. Clarsen, W. Derman, J. Dvorak, C. A. Emery, C. F. Finch, M. Häggglund, A. Junge, S. Kemp, K. M. Khan, S. W. Marshall, W. Meeuwisse, M. Mountjoy, J. W. Orchard, B. Pluim, K. L. Quarrie, B. Reider, M. Schwellnus, T. Soligard, K. A. Stokes, T. Timpka, E. Verhagen, A. Bindra, R. Budgett, L. Engebretsen, U. Erdener, K. Chamari, *Br. J. Sports Med.* **2020**, *54*, 372.
- [2] B. Y. Tan, T. Thach, Y. L. Munro, S. T. Skou, J. Thumboo, J. Car, L. T. Car, *Int. J. Environ. Res. Public Health* **2021**, *18*, 12757.
- [3] S. L. Sing, *Selective Laser Melting of Novel Titanium-Tantalum Alloy as Orthopaedic Biomaterial*, Springer, Berlin **2018**.
- [4] S. D. Dodds, A. Halim, *J. Hand Surg.* **2016**, *41*, e191.
- [5] T. T. Lögters, H. H. Lee, S. Gehrmann, J. Windolf, R. A. Kaufmann, *Hand* **2018**, *13*, 376.
- [6] M. H. Henry, *J. Am. Acad. Orthop. Surgeons.* **2008**, *16*, 586.
- [7] F. A. Russo, L. W. Catalano III, *Skeletal Trauma of the Upper Extremity*, Elsevier, Amsterdam **2022**, pp. 618–624.
- [8] P. Shetty, P. Yadav, M. Tahir, V. Saini, *Int. J. Oral Implantol. Clin. Res.* **2016**, *7*, 34.
- [9] M. Kaur, K. Singh, *Mater. Sci. Eng. C* **2019**, *102*, 844.
- [10] Z. Song, Q. Wang, T. Ma, C. Wang, N. Yang, H. Xue, Z. Li, Y. Zhu, K. Zhang, *J. Orthop. Surg. Res.* **2019**, *14*, 1.
- [11] J.-M. Kwak, K.-H. Koh, I.-H. Jeon, *Clin. Orthop. Surg.* **2019**, *11*, 369.
- [12] M. Pitta, C. I. Esposito, Z. Li, Y.-Y. Lee, T. M. Wright, *J. Arthroplasty* **2018**, *33*, 407.
- [13] C. K. Ledford, K. I. Perry, A. D. Hanssen, M. P. Abdel, *JAAOS-J. Am. Acad. Orthop. Surgeons* **2019**, *27*, 933.
- [14] L. Bian, N. Shamsaei, J. M. Usher, *Laser-Based Additive Manufacturing of Metal Parts: Modeling, Optimization, and Control of Mechanical Properties*, CRC Press, Boca Raton, FL **2017**.
- [15] Z. Wang, Y. Yang, *Biomed. Res. Int.* **2021**, *2021*, 6653967.
- [16] C. Garot, G. Bettega, C. Picart, *Adv. Funct. Mater.* **2020**, *31*, 2006967.
- [17] T.-S. Jang, D. E. Kim, G. Han, C.-B. Yoon, H.-D. Jung, *Biomed. Eng. Lett.* **2020**, *10*, 505.
- [18] M. Vignesh, G. Ranjith Kumar, M. Sathishkumar, M. Manikandan, G. Rajyalakshmi, R. Ramanujam, N. Arivazhagan, *J. Mater. Eng. Perform.* **2021**, *30*, 4735.
- [19] R. Hedayati, A. Leeftang, A. Zadpoor, *Appl. Phys. Lett.* **2017**, *110*, 091905.
- [20] L. Bai, C. Gong, X. Chen, Y. Sun, J. Zhang, L. Cai, S. Zhu, S. Q. Xie, *Metals* **2019**, *9*, 1004.
- [21] E. M. Guerrero, R. E. Baumgartner, A. E. Federer, S. K. Mithani, D. S. Ruch, M. J. Richard, *Hand* **2021**, *16*, 248.
- [22] C. Otto-Lambertz, A. Yagdiran, F. Wallscheid, P. Eysel, N. Jung, *Deutsches Ärzteblatt Int.* **2017**, *114*, 347.
- [23] M. Morgenstern, R. Kuehl, C. G. Zalavras, M. McNally, W. Zimmerli, M. A. Burch, T. Vandendriessche, W. T. Obreskey, M. H. J. Verhofstad, W. J. Metsemakers, *Bone Joint J.* **2021**, *103*, 213.
- [24] P.-H. Hsieh, M. S. Lee, K.-Y. Hsu, Y.-H. Chang, H.-N. Shih, S. W. Ueng, *Clin. Infect. Dis.* **2009**, *49*, 1036.
- [25] M. Cerioli, C. Batailler, A. Conrad, S. Roux, T. Perpoint, A. Becker, C. Triffault-Fillit, S. Lustig, M.-H. Fessy, F. Laurent, F. Valour, C. Chidiac, T. Ferry, *Front. Med.* **2020**, *7*.
- [26] A. Jaggessar, H. Shahali, A. Mathew, P. K. Yarlagadda, *J. Nanobiotechnol.* **2017**, *15*.
- [27] A. Jaggessar, A. Mathew, H. Wang, T. Tesfamichael, C. Yan, P. K. Yarlagadda, *J. Mech. Behav. Biomed. Mater.* **2018**, *80*, 311.
- [28] S. Pogodin, J. Hasan, V. A. Baulin, H. K. Webb, V. K. Truong, T. H. P. Nguyen, V. Boshkovikj, C. J. Fluke, G. S. Watson, J. A. Watson, R. J. Crawford, E. P. Ivanova, *Biophys. J.* **2013**, *104*, 835.
- [29] A. Velic, J. Hasan, Z. Li, P. K. Yarlagadda, *Biophys. J.* **2021**, *120*, 217.
- [30] H. Shahali, J. Hasan, A. Mathews, H. Wang, C. Yan, T. Tesfamichael, P. K. D. V. Yarlagadda, *J. Mater. Chem. B* **2019**, *7*, 1300.
- [31] A. Jaggessar, A. Mathew, T. Tesfamichael, H. Wang, C. Yan, P. K. Yarlagadda, *Molecules* **2019**, *24*, 1201.
- [32] Z. Jing, T. Zhang, P. Xiu, H. Cai, Q. Wei, D. Fan, X. Lin, C. Song, Z. Liu, *Biomed. Mater.* **2020**, *15*, 052003.
- [33] S. Attarilar, M. Ebrahimi, F. Djavanroodi, Y. Fu, L. Wang, J. Yang, *Int. J. Bioprinting* **2021**, *7*, 306.
- [34] G. Ng, A. Jarfors, G. Bi, H. Zheng, *Appl. Phys. A* **2009**, *97*, 641.
- [35] B. Zhang, Y. Li, Q. Bai, *Chinese J. Mech. Eng.* **2017**, *30*, 515.
- [36] D. Wang, Y. Wang, J. Wang, C. Song, Y. Yang, Z. Zhang, H. Lin, Y. Zhen, S. Liao, *Materials* **2016**, *9*, 608.
- [37] D. Wang, Y. Yang, R. Liu, D. Xiao, J. Sun, *J. Mater. Process. Technol.* **2013**, *213* 1734.

- [38] P. S. Kaliamoorthy, R. Subbiah, J. Bensingh, A. Kader, S. Nayak, *Rapid Prototyping J.* **2019**, 26, 319.
- [39] L. Thijs, F. Verhaeghe, T. Craeghs, J. Van Humbeeck, J.-P. Kruth, *Acta Mater.* **2010**, 58, 3303.
- [40] L. Ding, Z. Sun, Z. Liang, F. Li, G. Xu, H. Chang, *Metals* **2019**, 9, 1270.
- [41] J. Qazi, J. Rahim, O. Senkov, A. Genc, *Metall. Mater. Trans. A* **2001**, 32, 2453.
- [42] H. Bai, H. Deng, L. Chen, X. Liu, X. Qin, D. Zhang, T. Liu, X. Cui, *Metals* **2021**, 11, 534.
- [43] V. Anitha, A. N. Banerjee, S. W. Joo, B. K. Min, *Nanotechnology* **2015**, 26, 355705.
- [44] A. Jaggesar, P. Yarlagadda, K. D. V., *Adv. Mater. Lett.* **2020**, 11, 1.
- [45] B. Baufeld, O. Van der Biest, *Sci. Technol. Adv. Mater.* **2009**, 10, 015008.
- [46] K. Karolewska, B. Ligaj, in *AIP Conf. Proc.*, Vol. 2077, AIP Publishing LLC February 21 **2019**, p. 020025.
- [47] R. Sabban, S. Bahl, K. Chatterjee, S. Suwas, *Acta Mater.* **2019**, 162, 239.
- [48] A. Velic, J. Hasan, Z. Li, P. Yarlagadda, *Biophys. J.* **2021**, 120, 217.
- [49] A. Velic, A. Jaggesar, T. Tesfamichael, Z. Li, P. K. Yarlagadda, *Nanomaterials* **2021**, 11, 2472.
- [50] J. Jenkins, J. Mantell, C. Neal, A. Gholinia, P. Verkade, A. H. Nobbs, B. Su, *Nat. Commun.* **2020**, 11, 1.
- [51] M. Olivi, E. Zanni, G. De Bellis, C. Talora, M. S. Sarto, C. Palleschi, E. Flahaut, M. Monthieux, S. Rapino, D. Uccelletti, S. Fiorito, *Nanoscale* **2013**, 5, 9023.